Energy Reports 8 (2022) 8675–8689

Contents lists available at ScienceDirect

Energy Reports

journal homepage: www.elsevier.com/locate/egyr

Research Paper

Interference mechanism in coalbed methane wells and impacts on infill adjustment for existing well patterns

Qifeng Jia [a,b,e], Dameng Liu [a,b,*], Xiaoming Ni [c], Yidong Cai [a,b], Yuejian Lu [a,b], Zongyuan Li [d], Yingfang Zhou [e]

[a] School of Energy Resources, China University of Geosciences, Beijing 100083, China
[b] Coal Reservoir Laboratory of National Engineering Research Center of CBM Development & Utilization, China University of Geosciences, Beijing 100083, China
[c] School of Energy Science and Engineering, Henan Polytechnic University, Jiaozuo, Henan 454000, China
[d] PetroChina Huabei Oilfield Company, Renqiu, Hebei 062550, China
[e] School of Engineering, Fraser Noble Building, King's College, University of Aberdeen, AB24 3UE Aberdeen, UK

ARTICLE INFO

Article history:
Received 2 February 2022
Received in revised form 12 May 2022
Accepted 22 June 2022
Available online 4 July 2022

Keywords:
Well interference
Coalbed methane
Permeability
Infilling
Gas diffusion dynamics

ABSTRACT

Inter-well interference, a superimposed effect of pressure propagation from adjacent wells, can enhance the dynamics of methane desorption in pores and gas transport in fractures through energy migration. To better understand the variation pattern of seepage efficiency, the inter-well interference mechanism of different types of reservoirs and productivity changes after infilling coalbed methane wells were investigated. The results showed that the average productivity of old wells increased by 627 m^3/d after infilling a horizontal well in the high-permeability reservoirs without surrounding rock water supply (HP-WW); however, the newly infilled horizontal well produced gas at 4996 m^3/d. The infill well in HP-WW reservoir resulted in 11-39permeability increment compared with initial permeability (the average permeability changes from 1.58 to 2.18 mD). While, much higher permeability increment was observed (varies from 29-50) in relative low permeability coalbed formation due to infill well. After the formation of interference, increased confining pressure increases effective stress, which is smaller than the positive effect formed by the fracture expansion and the increase in the effective diffusion area. Additionally, well interference promotes coupled superposition of the pressure drop funnel, which effectively suppresses the influence induced by velocity sensitivity, water sensitivity, and water lock, resulting in an increased pressure difference between the reservoir and the wellbore. This enhances the dynamics of methane desorption from the pore surface and gas migration from the fracture. For gas diffusion, the mean free path of gas molecules decreases with well interference, implying that the main diffusion resistance changes from collisions between gas molecules and the pore wall to collisions among gas molecules. Therefore, the findings of this study can help for better understanding of the response mechanism of inter-well interference to efficient CBM production.

1. Introduction

The efficient development and utilization of coalbed methane (CBM) are crucial in unconventional oil and gas exploration that helps to improve the safety of coal mines and alleviate the gap between energy supply and demand (Wayne, 2003; Majdi et al., 2012). Increasing the desorption volume is important for increasing CBM production in well pattern development, primarily due to the formation of inter-well interference (Connell et al., 2016; Davudov and Moghanloo, 2018; Yang et al., 2018a). The multi-period, diversity, and variability of the coal-forming environment in China determine the strong heterogeneity of CBM reservoirs (Guo et al., 2017), leading to complex inter-well interference patterns in CBM exploitation (Fig. 1). Presently, the primary methods for evaluating CBM inter-well interference include dynamic production analysis, interference well testing, and theoretical judgment (Liu et al., 2018a; Xu and Wang, 2017; Kumar et al., 2016; Wang and Qin, 2019). Among these, the production dynamic analysis method is typically used to determine the degree of inter-well interference by comparing and analyzing the gas–water production of CBM wells that have minor differences in reservoir conditions, fracturing methods, and well spacing (Yang et al., 2019). However, inter-well interference can only be qualitatively analyzed, and therefore, the extent of

* Corresponding author at: School of Energy Resources, China University of Geosciences, Beijing 100083, China.
E-mail address: dmliu@cugb.edu.cn (D. Liu).

https://doi.org/10.1016/j.egyr.2022.06.070

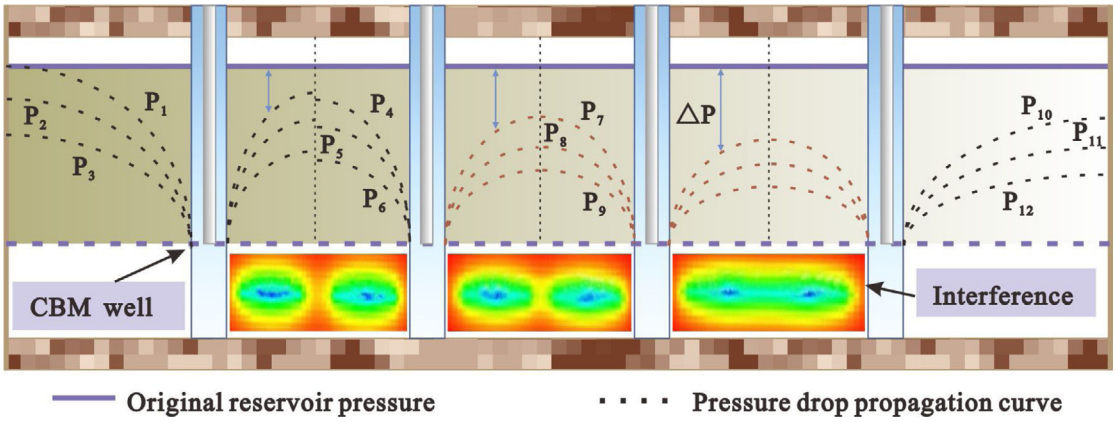

Fig. 1. The general sketch of inter-well interference.

interference cannot be quantified. In the interference well testing, highly sensitive electronic pressure gauges are installed in both the test and the observation wells. The test well operating system is subjected to continuous variations (Cramer et al., 1999). Pressure changes in the observation well are then measured, and the changes in the test well drainage are simultaneously monitored to determine the extent of interference between the wells (Hoffman and Caers, 2005; Clarkson, 2009; Meng et al., 2018; Pashin, 2007). This method is more accurate for determining the degree of inter-well interference and is therefore widely used in many CBM development blocks (Andrew et al., 2006; Wang et al., 2019). However, the long shut-in time required for the test does not facilitate the continuous drainage of the CBM wells. The theoretical judgment method is used to analyze the degree of inter-well interference by establishing a pressure drop funnel model based on reservoir hydrodynamic conditions, daily water production, and permeability and then comparing the changes before and after superposition (Shi et al., 2018; Rice et al., 2008). This method is theoretically more systematic in analyzing the interference situation, and the establishment of the superimposed pressure drop funnel model has been accepted by many researchers (Reeburgh et al., 2006; Smith et al., 1982). However, owing to the elastic self-regulation effect caused by stress sensitivity and matrix shrinkage in coal reservoirs, developing a realistic pressure drop funnel model is challenging.

The adjustment of CBM well pattern is not only a vital part of the CBM development scheme but also a significant link in CBM exploitation projects (Majdi et al., 2012; Wang et al., 2016; Moore, 2012; Palmer, 2009). Previous studies on well pattern adjustment have primarily focused on well pattern density and layout orientation (Mazumder et al., 2012; Smith and Pallasser, 1996). A lower well pattern density can lead to ineffective inter-well interference, affecting the methane diffusion-seepage rates (Clarkson, 2009; Clarkson and Qanbari, 2016; Dejam et al., 2018). The smaller the well spacing, the fewer resources to be controlled by a single well, resulting in earlier depletion of gas sources in reservoirs with high permeability and better fracture conductivity (Aminian and Ameri, 2009; Zhang et al., 2018; Mora and Wattenbarger, 2009). As the extensional characteristics of hydraulic fractures in coal reservoir reconstruction directly affect the pressure drop propagation and gas migration path of the CBM wells (Salmachi and Karacan, 2017), well patterns are generally arranged along the long axis, either parallel to the hydraulic fracture or perpendicular to the butt cleat direction.

As shown in the literature, previous work for the analysis of inter-well interference was mainly based on the judgment of the black-box model or the conjecture from field experience (Wang et al., 2018; Zhao et al., 2016). Interestingly, the study of inter-well interference by variations in carbon isotope, hydrogen isotope or CBM composition provides new insights into low-permeability reservoirs (Jia et al., 2021; Liu et al., 2018a; Shi et al., 2018), which gives good implications for flow field changes during drainage (Karacan, 2013). According to the fluid transport characteristics (Yang et al., 2018a), the elastic energy model of CBM established by considering the free and adsorption states shows that the critical factors affecting inter-well interference include reservoir pressure gradient, effective stress and drainage system (Ju et al., 2021; Ni et al., 2019; Wang and Qin, 2019). However, considering inter-well interference, reasonable well spacing for different types of reservoirs in inefficient areas is not quantified. After infilling horizontal and vertical wells in the exploited CBM well pattern area, the interference promotion mechanism has not been published, especially regarding the weakened reservoir sensitivity. This study fully considered the difference between the original and post-fracturing permeability and constructed mathematical models of pressure propagation that were more consistent with objective reality. Based on the drainage characteristics of high or low permeability reservoirs, inter-well interference was characterized by combining field data with numerical simulations, followed by quantifying the optimal well spacing for different types of reservoirs. Aiming at the multi-period, diversity and variability of coal-forming environments, the suppression effect of reservoir sensitivity (velocity sensitivity, water sensitivity, and water lock) after infilling horizontal and vertical wells in the well pattern was evaluated, which was not reported in previous studies.

This study first presents the geological background of the southern Qinshui Basin, and then simulates the degree of inter-well interference and productivity changes for two typical reservoirs. To further analyze the geological fluid effects of CBM production, the change law of methane seepage after infilling horizontal and vertical wells in the well pattern was evaluated, followed by the verification of the analysis of CBM production through successful field cases. For fluid transport behavior in pore-fracture channels, the suppression effect of inter-well interference on coal reservoir sensitivity and the mechanism of promoting gas diffusion are revealed. Therefore, this research provides new insights into the fluid dynamics of unconventional reservoirs and the dynamic geological effects of CBM production.

2. Geological setting

2.1. Structures

The southern Qinshui Basin, located in the Jincheng slope zone, is the most active area for CBM exploration and development

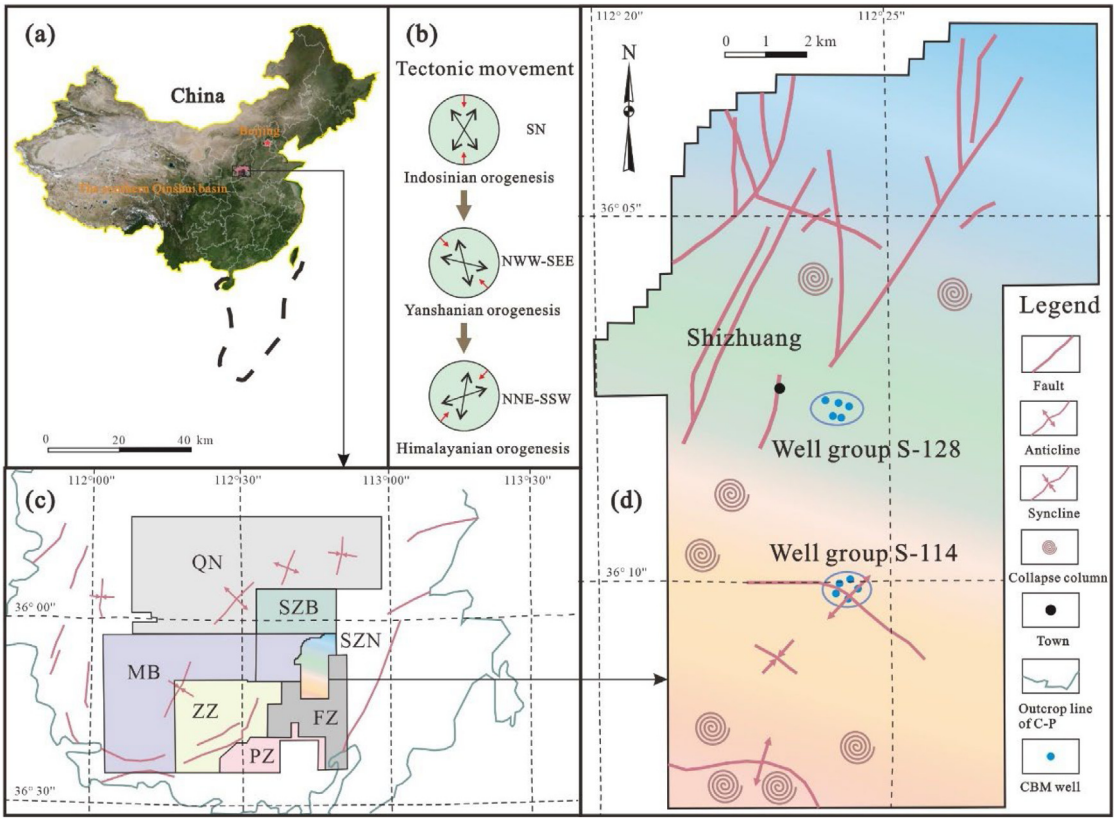

Fig. 2. Geographical position and tectonic outline map of the Shizhuangnan Block in the southern Qinshui Basin, China. (a) Location of the study area in China; (b) Tectonic movements of the southern Qinshui basin; (c) CBM development blocks in the southern Qinhsui basin; (d) Structure outline of the Shizhuangnan Block. SZN, Shizhuangnan CBM Block; SZB, Shizhuangbei CBM Block; QN, Qinnan CBM Block; MB, Mabi CBM Block; ZZ, Zhengzhuang CBM Block; PZ, Panzhuang CBM Block; FZ, Fanzhuang CBM Block.

in China (Wang et al., 2016; Zhang et al., 2018; Kang et al., 2020). It has abundant Carboniferous and Permian coal resources, with a coal reserve of approximately 2.7×10^{11} t. This area has undergone multi-stage tectonic movements since the Indosinian movement, forming a wide syncline with an almost NNE trend (Wang et al., 2019; Zhang et al., 2018). The geographical position and tectonic outline map of the Shizhuangnan Block are shown in Fig. 2. This block remained stable during the Indosinian movement, despite being squeezed by tectonic stresses in the near SN direction, and no distinct geological structures were formed. The major tectonic activity during the Yanshanian movement showed extrusive uplift, resulting in the formation of a broad fold that trends along the NE–NNE within the basin, with a series of secondary folds developing on both flanks of the folds (Cai et al., 2011). During the Himalayan movement, a reversal of tectonic stresses (stress relaxation occurred along the NNE-SSW with the maximum extrusion stress), manifested as tensile stresses, led to a corresponding negative reversal of the pre-formed extrusive structures, resulting in smaller-scale anticlines and synclines and secondary broad and gentle folds superimposed on the Yanshanian (Liu et al., 2018a). Additionally, regional linear structures are well developed; most of the anticlines have short axes of only 1–3 km, whereas the long axis extends over 100 km. The faults within the basin are less developed and are divided into several types, including parallel displacement faults, high-angle normal/reverse faults, and medium-low angle reverse faults, all of which have small fault displacements and short extensions. Influenced by the tectonic movements of the Indosinian, Yanshanian, and Himalayan (Guo et al., 2017; Kang et al., 2020; Meng et al., 2018), the physical and chemical properties of the coal seams in the area are quite different. Although the degree of the thermal evolution of coal under good hydrodynamic conditions and large overlying effective thickness is generally high, the CBM reservoirs exhibit strong heterogeneity, particularly for gas content, cleats, and permeability (Cai et al., 2011).

2.2. Coal-bearing strata

The coal-bearing strata in the study area belong to the Carboniferous-Permian System, which includes the Benxi (BXF), Taiyuan, Shanxi Lower Shihezi, Upper Shihezi, and Shiqianfeng Formations from bottom to top, respectively (Wang et al., 2016; Zhang et al., 2018). Among these, the Shanxi and Taiyuan Formations are the main coal-bearing strata, which have independently developed to one stable and mineable coal seam, namely coal seams $3^{\#}$ and $15^{\#}$ (Fig. 3). The coal seams of the Shanxi Formation are generally thick in the south and thin in the north, whereas those of the Taiyuan Formation are the opposite (Cai et al., 2014). Regarding sediment characteristics, the Shanxi Formation strata developed in the delta deposition above the epicontinental sea sedimentary background, generally transitioning from the delta estuary bar and tributary bay to the delta plain facies, thereby developing a suite of coal-bearing rock systems based on delta deposition and dominated by mudstone, siltstone, and fine-grained sandstone (Liu et al., 2018b). The Taiyuan Formation strata formed a composite sedimentary system of the tidal flats–lagoons–barrier islands–carbonate platform with intersecting land and sea, comprising mudstones, siltstones, fine-grained sandstones, limestones, and coal seams.

Table 1
Sample information and basic parameters of the selected coals.

Samples	$R_{o,max}$ (%)	Per (mD)	Proximate analysis (%)				Coal maceral composition (%)		
			M_{ad}	A_{ad}	V_{ad}	FC_{ad}	V	I	E
S-128	1.86	1.2	0.55	18.26	7.68	73.51	91.7	7.1	1.2
S-024	2.11	1.8	0.46	17.62	8.16	73.76	97.3	2.7	0
S-025	2.03	1.7	0.39	23.15	7.21	69.25	96.2	3.8	0
S-129	1.95	1.1	0.52	20.36	8.87	70.25	90.1	9.6	0.3
S-031	2.28	2.1	0.38	22.15	6.32	71.15	93.6	6.4	0
S-114	1.26	0.5	1.22	9.91	18.92	69.95	81	15.8	3.2
S-115	1.31	0.3	1.36	8.28	20.13	70.23	86.2	12.5	1.3
S-010	1.02	0.1	1.41	10.28	15.37	72.94	74.5	18.8	6.7
S-016	1.35	0.4	1.19	11.37	19.18	68.26	84.3	13.1	2.6
S-131	1.41	0.5	0.99	7.01	21.66	70.34	90.2	9.8	0

Note: $R_{o,max}$, maximum vitrinite reflectance; Per, permeability; M_{ad}, moisture (air-dried basis); A_{ad}, ash (dry basis); V_{ad}, volatile matter (dry, ash-free basis); FC_{ad}, Fixed carbon (air-dried basis); V, vitrinite; I, inertinite; E, exinite.

3. Methodology

3.1. Coal sampling and basic analysis

Coal samples from drilling cores obtained from 10 CBM wells in the Shizhuangnan Block were used in this study. All samples were carefully wrapped and immediately sent to the laboratory for basic analyses, including maximum vitrinite reflectance estimation, proximate analysis, and coal maceral composition analysis following the ISO 7404.3-1994, ISO 17246-2010, and ISO 7404.5-1994 standards, respectively. The detailed experimental equipment and procedures have been reported in our previous study (Cai et al., 2018). The permeability values obtained via the pressure pulse attenuation method ranged from 0.1 to 2.1 mD (Table 1), indicating the possible existence of multi-stage microfractures (Cai et al., 2011; Palmer, 2009). The proximate analysis provided the following: 0.38%–1.41% moisture (air-dried basis), 7.01%–23.15% ash (dry basis), 6.32%–21.66% volatile matter (dry, ash-free basis), and 68.26%–73.76% fixed carbon (air-dried basis). To minimize the evolution of drying artifacts, we employed high-pressure freezing and subsequent freeze-drying, which was the same as the drying process described by Keller et al. (2016).

3.2. Classification of reservoir types

The CBM well drainage control process in China primarily uses three technical methods: slow and steady fine drainage, five-section three-pressure drainage (the drainage is divided into five stages: single-phase water flow, gas–water two-phase flow and low gas production, stable gas production, constant pressure production, and depletion), and double-pressure box six-section drainage (the drainage is divided into six stages: balanced drainage, pressure-relief drainage, moderate-hold-pressure drainage, gradual production release, stable gas production, and attenuation phase). The slow and steady fine drainage and five-section three-pressure drainage methods have been widely used, whereas the double-pressure box-type six-section drainage method has been used in the development of a small number of horizontal wells. Regardless of the type of drainage system used, the coal seam is considered a type of reservoir without the surrounding rock water supply (WW), under the condition that the daily water output has been low since the start of drainage (Yang et al., 2018a; Wang et al., 2019), or that the upper and lower surrounding rocks adjacent to the coal seam are mudstones greater than 5 m in thickness (Fig. 3, or that the thickness of the mudstone ranges from 3 to 5 m, with a cumulative water output less than 2000 m^3 in five years (Yang et al., 2018a; Liu et al., 2018a; Ni et al., 2021). Additionally, because coal seams with permeabilities exceeding 1 mD are considered as high-permeability reservoirs, according to Kang et al. (2020), we divided the coal seams into the high-permeability reservoirs without surrounding rock water supply (HP-WW) and low-permeability reservoirs without surrounding rock water supply (LP-WW). Because the boundary of the coal seam that is replenished by water from the surrounding rock is not clear, we did not investigate this situation in this study.

A geological model was established based on the analysis of a large amount of logging and coal core test data. The three-dimensional structure and attribute models of the coal reservoir were simulated using both sequential Gaussian simulation and multiple linear statistics (Liu et al., 2018b). Furthermore, two well groups were selected from each type of reservoir (well groups S-128 and S-144 belonged to HP-WW and LP-WW, respectively), and the degree of well interference was evaluated by importing the basic parameters of each well.

3.3. Well interference simulation

There are two fluid phases in a coal reservoir: gas and water. The CBM is primarily stored on the inner surface of the matrix micropores in an adsorbed state, and there is no water in the matrix micropores (Harrison et al., 2006). Considering the diffusion term, the gas-phase and water-phase seepage equations are as follows (Karacan, 2013; Guo et al., 2017; Wang et al., 2019):

$$\frac{\partial(\rho_g S_g \phi)}{\partial t} = \nabla\left[\frac{KK_{rg}\rho_g}{\mu_g}\nabla(p_g - \rho_g g H) + \frac{\rho_g D_f}{C_f}\nabla C_f\right] \quad (1)$$

$$\frac{\partial(\rho_w S_w \phi)}{\partial t} = \nabla\left[\frac{KK_{rw}\rho_w}{\mu_w}\nabla(p_w - \rho_w g H)\right] \quad (2)$$

where K is the absolute permeability of the coal rock, K_{rg} and K_{rw} are the relative permeabilities of gas and water, respectively; S_g and S_w are the gas and water saturation values, respectively; p_g and p_w are the gas and water pressures in the fracture system, respectively; ρ_g and ρ_w are the densities of gas and water, respectively; μ_g and μ_w are the viscosities of gas and water in the fracture system, respectively. D_f is the diffusion coefficient; C_f is the volume concentration; g is the acceleration due to gravity. H is the depth calculated from the base level; φ is the porosity of coal-rock; and t is the seepage time.

The permeability varies with porosity as (Clarkson and Qanbari, 2016):

$$\frac{K}{K_0} = \left(\frac{\varphi}{\varphi_0}\right)^n \quad (3)$$

where K_0 and φ_0 are the initial permeability and porosity, respectively.

The auxiliary equations and boundary conditions are as follows (Ibrahim and Nasr-El-Din, 2015; Mora and Wattenbarger,

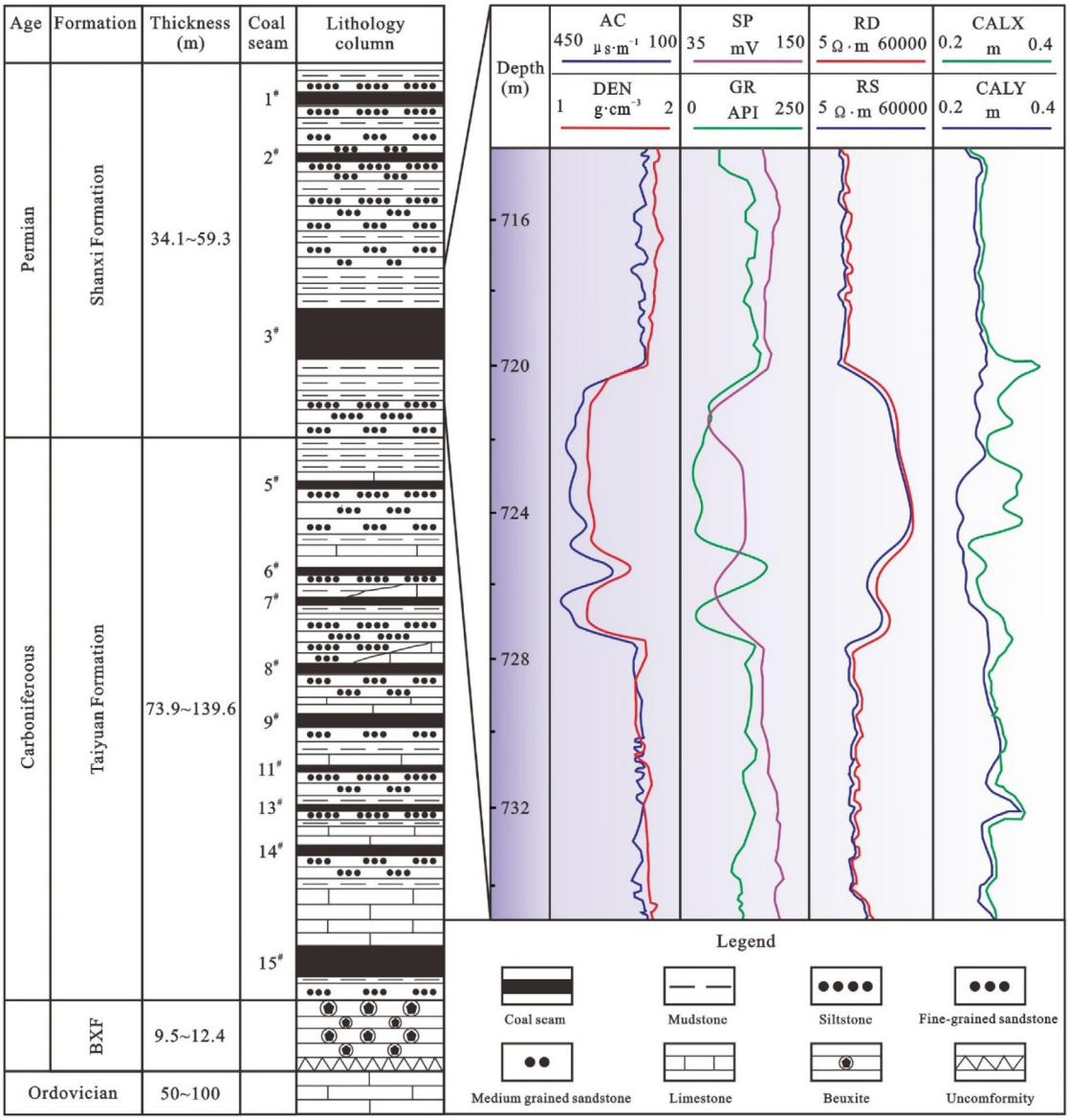

Fig. 3. Stratigraphic column of coal-bearing sequence and geophysical logging curves of coal seam 3# in the Shizhuangnan Block.

2009):

$$\begin{cases} S_g + S_w = 1 \\ p_c(S_w) = p_g - p_w \end{cases} \tag{4}$$

$$\begin{cases} p|_{r_w} = p_{wf}(x, y, z, t) \\ p|_{\Gamma} = f(x, y, z, t) \end{cases} \tag{5}$$

where P_c (S_w) is capillary pressure; $p\ |_{r_w}$ is the pressure at the bottom of the hole. p_{Wf} (x, y, z, t) is the value of the bottom hole pressure at time t; $p\ |_{\Gamma}$ is the value of the pressure at the gas reservoir boundary; and f (x, y, z, t) is a given function of the pressure p at time t.

In the established structural grid, assuming that each grid is perforated, the total output across n grids can be expressed as follows (Meng et al., 2018; Ibrahim and Nasr-El-Din, 2015; Wang et al., 2019):

$$q_{w,h} = \sum_{1}^{n} T_{w,i} M_{p,i} \Delta P = 2T_{w,i} M_{p,i} (p_e - p_{wf}) \quad (i = 1, 2, 3, 4, 5, 6\ldots) \tag{6}$$

where $q_{w,h}$ is the total output; $T_{w,i}$ is the conductivity of each grid. $M_{p,i}$ is the fluidity ratio of the fluid in the ith grid; p_e is the formation pressure; and p_{wf} is the pressure at the grid where the root is located.

During CBM well drainage, the water and gas production rates vary among the four stages, resulting in different water-pressure transmission conditions in each drainage stage. The mathematical models of hydraulic pressure propagation in the four drainage stages were developed based on the fracture extension length, original permeability, and post-fracture permeability. According to the revised Kusakin formula, the long-axis influence radius (R_{x1}) and short-axis influence radius (R_{y1}) at the single-phase flow stage can be expressed as follows (Harrison et al., 2006; Cai et al., 2014; Ibrahim and Nasr-El-Din, 2015; Wang et al., 2019):

$$R_{x1} = 2S_1\sqrt{hk_{d1}} + 2S_{x1}\sqrt{\frac{hk_{lc}\rho_w g}{\mu_w}} + 2(S_0 - S_1 - S_{x1})\sqrt{\frac{hk_0\rho_w g}{\mu_w}} \tag{7}$$

$$R_{y1} = 2S_{x1}\sqrt{\frac{hk_c\rho_w g}{\mu_w}} \tag{8}$$

where S_0 is the drawdown of the hydrodynamic surface at the single-phase flow stage of drainage; S_1 is the drawdown in the effective support range; S_{x1} is the drawdown in the long-axis fracture extension direction without effective support. h is the thickness of the aquifer. k_{d1} is the permeability coefficient in the support range; k_{lc} is the permeability of the long-axis fracturing section without effective support. k_c is the permeability after fracturing; μ is the viscosity coefficient of water.

When the bottom hole pressure reaches the critical desorption pressure, CBM begins to desorb and is produced at a faster rate. Simultaneously, water and gas in the coal seam jointly occupy the fracture channels. To allow water from the far end of the wellbore to flow toward the near-wellbore area, the gas–water two-phase flow and low gas production stage, a drainage mode that uses holding pressure in the early stage and produces low gas in the late stage, is generally adopted. The long-axis influence radius (R_{x2}) and short-axis influence radius (R_{y2}) can be expressed as follows (Wang et al., 2019):

$$R_{x2} = 2S_{x2}\sqrt{\frac{hk_0 \times 0.0027e^{6.2144S_w}\rho_w g}{\mu_w}} \tag{9}$$

$$R_{y2} = 2S_{dg1}\sqrt{hk_c \times 0.0027 \times e^{6.2144S_w}\rho_w g} + 2(S_{x2} - S_{dg1}) \times \sqrt{\frac{hk_0 \times 0.0027 \times e^{6.2144S_w}\rho_w g}{\mu_w}} \tag{10}$$

where S_{x2} is the drawdown in the low gas production stage and S_{dg1} is the drawdown in the gas–water two-phase flow.

As the bottom hole pressure is further reduced, a certain desorption radius is formed in the coal reservoir, and the drainage process gradually enters the stage of stable gas production. Thus, the produced gas further impedes the water flow, resulting in a further decrease in the relative permeability of the water phase, similar to the characteristics of the gas–water two-phase flow and low gas production stage. Therefore, the model of pressure propagation in the stable gas production stage is similar to that in the low gas production stage and is thus not repeated here.

As the bottom hole pressure cannot drop indefinitely, the pressure change value is minimal when it reaches the limit value, at which point, the CBM well drainage process is in a constant pressure production stage. Thus, the water pressure begins to propagate longitudinally with the drainage process, while the water outside the boundary is fed from within the boundary in the horizon owing to pressure difference. Therefore, the influence radii R_{x3} and R_{y3} in the long-axis and short-axis directions at the constant pressure production stage can be obtained as follows (Wang et al., 2019):

$$R_{x3} = 196 \times (a_x \ln t_{rcg} + b_x)\sqrt{\frac{hk_{rwc}\rho_w g}{\mu_w}} \tag{11}$$

$$R_{y3} = 196 \times (a_y \ln t_{rdg} + b_y)\sqrt{\frac{hk_{rwd}\rho_w g}{\mu_w}} \tag{12}$$

where t_{rcg} is the time of constant pressure in the long-axis direction during the constant pressure stage; t_{rdg} is the time of constant pressure in the short-axis direction during the constant-pressure stage. a_x and b_x are the fitting coefficients of the pressure drop in the long-axis direction; a_y and b_y are the fitting coefficients of the pressure drop in the short-axis direction; k_{rwc} and k_{rwd} are the water-phase relative permeabilities in the long-axis and short-axis directions, respectively.

3.4. Productivity fitting

Based on the well interference model, production histories of all CBM wells were fitted in conjunction with the formation fluid parameters using well logs, while the accuracy of the established well interference model was validated using the degree of fitting (see Fig. 4 for the fitting procedure). Additionally, the dynamic parameters were fitted to remove any gas production anomalies caused by coal powder blockage, gas engine failure, and replacement of the frequency converter.

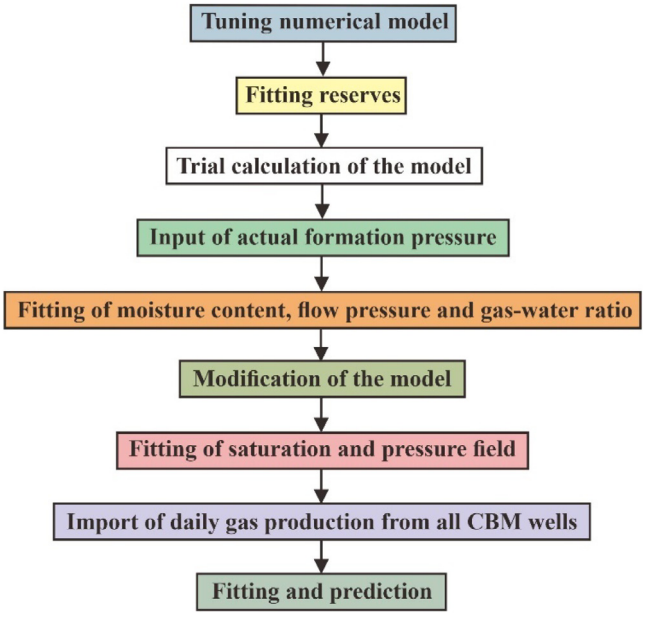

Fig. 4. Procedures for model fitting and prediction.

4. Results and discussion

4.1. Reservoir well interference

The formation of inter-well interference is crucial for the vertical expansion of the pressure drop funnel in a single well and the superposition coupling of pressure drop propagation in adjacent wells. Previous studies (Guo et al., 2017; Liu et al., 2018a) have revealed that CBM wells in China generally form well interference in the middle or later drainage stages. Fig. 5 shows the pore-fluid pressure propagation of HP-WW and LP-WW reservoirs. No inter-well interference was observed when the two well groups started producing gas (Fig. 5a$_1$ and b_1). However, wells S-025, S-031, S-129, and S-024, belonging to the HP-WW reservoir, formed inter-well interference along the long-axis (Fig. 5a$_2$), while no interference was observed in the LP-WW (Fig. 5b$_2$); this is consistent with the results of Liu et al. (2018a) and Yang et al. (2019). As shown in Fig. 5a$_1$ and a_2, the average pore-fluid pressure of well group S-128 varied from 2.5 to 0.5 MPa over the course of gas production, indicating that the HP-WW had higher pressure propagation efficiency with a faster pressure drop funnel superposition rate. However, Fig. 5b$_1$ and b_2 reveal that the average pore-fluid pressure of well group S-114 ranged 2.0–0.7 MPa at the same drainage time, which suggests a lower methane desorption efficiency in the LP-WW, indicating high propagation resistance of that fracture.

As shown in the well test results in Table 2, well S-031 in the HP-WW received an interference signal from test well S-025, which indicated that inter-well interference was formed in the HP-WW. However, no interference signal was received by the CBM wells in the LP-WW, indicating that no inter-well interference was formed. These results correspond with the above-mentioned results, confirming the accuracy of the numerical simulation results.

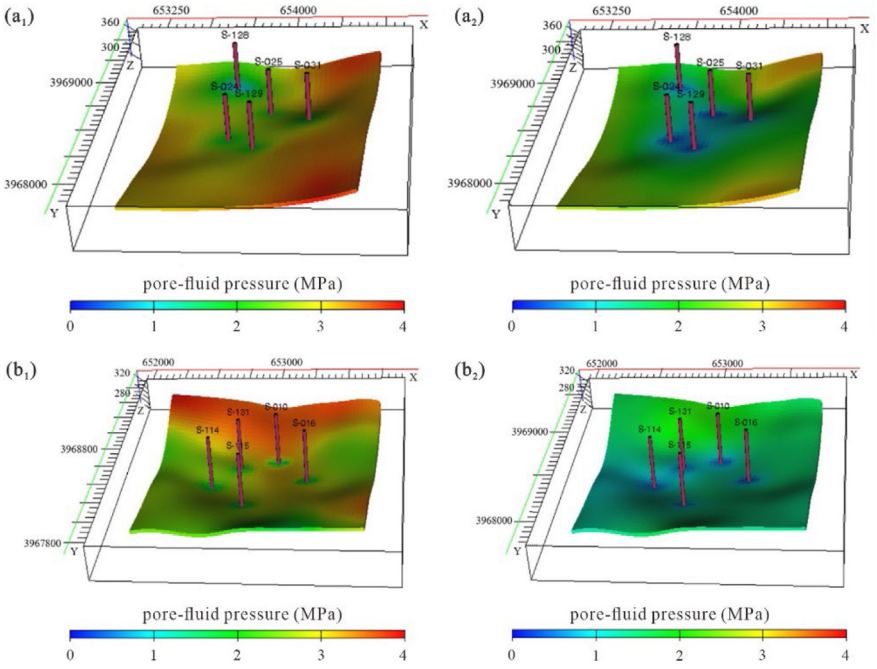

Fig. 5. Variation in pore-fluid pressure propagation in the HP-WW and LP-WW reservoirs. (a_1) and (a_2) are inter-well interference models for well group S-128 at the start of gas production and present day, respectively; (b_1) and (b_2) are inter-well interference models for well group S-114 at the beginning of gas production and present day, respectively. There was no inter-well interference when the two well groups started to produce gas, but now wells S-025 and S-031, S-129 and S-024, belonging to the HP-WW reservoir, form inter-well interference along the long-axis, respectively. In contrast, no interference is formed in the LP-WW reservoir.

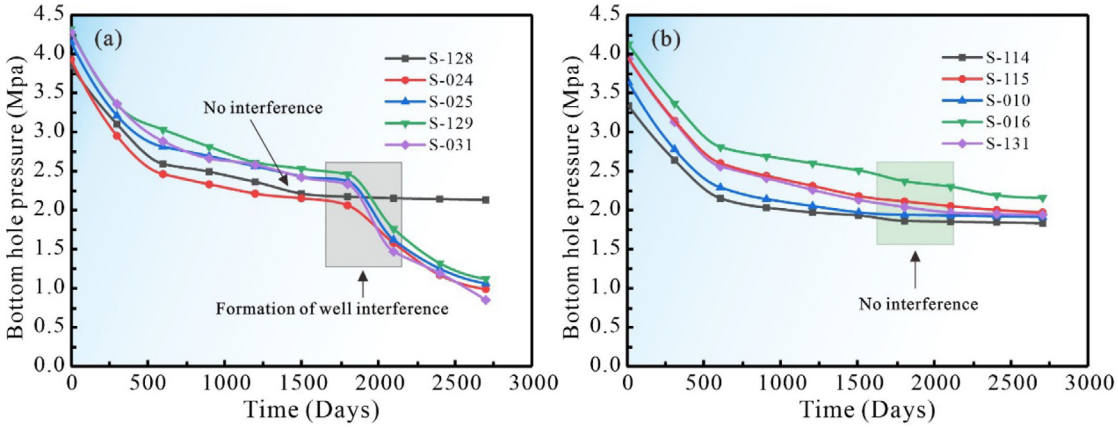

Fig. 6. Changes in bottom hole pressure with drainage time. (a) shows a change in the trend of bottom hole pressure after the formation of wells interference in well group S-128; (b) indicates a general logarithmic decrease in bottom hole pressure with drainage time for well group S-114.

Table 2
Test results from interfered well tests.

Wells	CST (m)	RP (MPa)	WS (m)	BHP (MPa)	WP (m^3/d)	MDFD	IS
S-128	6.12	4.19	307	2.11	0.5	NE53°	Not received
S-024	6.33	3.98	318	0.83	0.6	NE49°	Not received
S-025	6.27	4.26	–	0.91	0.8	NE59°	Test well
S-129	5.95	4.51	371	1.06	0.5	NE52°	Not received
S-031	6.88	4.75	260	0.81	0.9	NE53°	Received
S-114	5.7	3.68	362	1.79	0.3	NE50°	Not received
S-115	6.03	4.23	–	1.92	0.7	NE58°	Test well
S-010	5.98	3.63	486	1.85	0.2	NE48°	Not received
S-016	6.15	4.39	479	2.13	0.9	NE52°	Not received
S-131	5.86	4.12	472	1.88	0.6	NE53°	Not received

Note: CST, coal seam thickness; RP, reservoir pressure; WS, well spacing; BHP, bottom hole pressure; WP, water production; MDFD, the main direction of fracture development; IS, interference signal.

In the CBM drainage process, the bottom hole pressure reflects the reservoir pressure drop propagation rate and CBM desorption efficiency (Wang et al., 2019). As shown in Fig. 6a, the bottom hole pressure initially decreased rapidly with drainage time and then stabilized; however, wells S-024, S-129, S-025, and S-031 exhibited another sharp downward trend in bottom hole pressure after the formation of inter-well interference, indicating significant productivity increases in the interfering wells. Figs. 6b and 7b show that both bottom hole pressure and water production generally decreased with drainage time before the formation of inter-well interference. This phenomenon is detrimental to the desorption of CBM in the reservoir located away from the wellbore, leading to fracture plugging. For interfering CBM wells, the pressure drop funnels were vertically and laterally superimposed on each other, causing changes in the reservoir seepage and stress fields that resulted in changing trends for both the bottom hole pressure and water production.

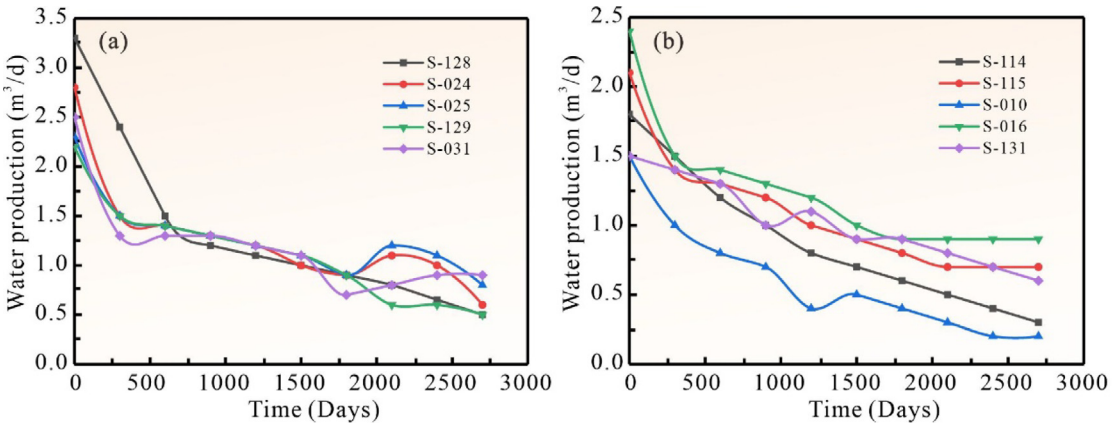

Fig. 7. Changes in water production with drainage time. (a)- well group S-128; (b)- well group S-114.

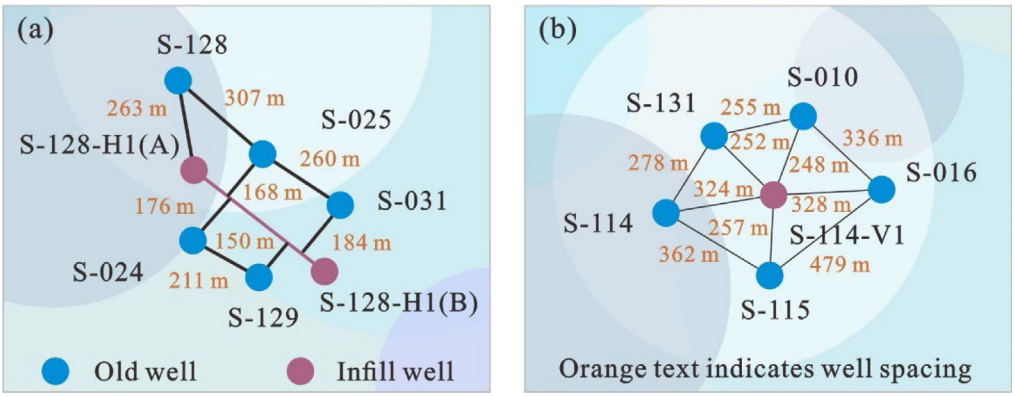

Fig. 8. The layout of different types of infilled wells. (a) and (b) indicate the infill of a horizontal well in well group S-128 and a vertical well in well group S-114, respectively.

4.2. Infill adjustment for well patterns

4.2.1. Horizontal wells

Compared with those of vertical wells, both the reservoir pressure-propagation distance and pressure-relief range are longer for horizontal wells after infilling; however, better geological conditions and complex infilling mining technologies are required (Zhang et al., 2018; Liu et al., 2020). Herein, the coal seam thickness of the well group S-128 varied from 5.95 to 6.88 m, the well depth ranged 685–725 m, and the gas content, controlled by the NEE–SWW oriented compressional stress field, ranged 10.23–22.43 m^3/t. In addition, most of the adjacent wells were spaced more than 250 m apart, resulting in relatively low overall gas production. There is no large fault or collapse column near this well group, whose structure is relatively simple, whose structure is relatively simple and whose coal quality is good (primarily cataclastic coal), indicating high potential for gas production from this well group. Thus, the well group S-128 is suitable for infilling a horizontal well to achieve inter-well interference (as shown in Fig. 8a). This disrupts the original equilibrium in the reservoir, thereby increasing the production of the interfering wells.

Fig. 9 illustrates the actual daily gas production and simulation fitting results of well group S-128 during the drainage process. The drainage conditions are as follows: wells S-129 and S-031 have relatively high gas production, both above 1000 m^3/d (see Fig. 9d and e), whereas other wells have less than satisfactory gas production, as shown in Fig. 9a, c, and d. The reservoirs in wells S-128, S-025, and S-0129 experienced severe fracture channel blockage by coal powder, resulting in reduced reservoir gas propagation efficiency. Another interesting phenomenon was the sudden increase in excessive gas production that occurred in wells S-024, S-025, S-129, and S-031 during the mid-drainage phase, increasing from 155 to 1595 m^3/d, 130 to 962 m^3/d, 270 to 1405 m^3/d, and 208 to 1953 m^3/d (as shown in Fig. 9b, c, d, and e), respectively. This indicated that the four wells formed inter-well interference, resulting in the superposition of pressure drop propagation and facilitating CBM desorption, thereby increasing the productivity of the other wells.

As shown in Fig. 9, the productivity of all the old wells increased after a horizontal well in well group S-128 was infilled. The productivity of wells S-128, S-024, S-025, S-129, and S-031 increased by 640, 887, 822, 376, and 409 m^3/d, respectively, while the newly infilled horizontal well produced gas at 4996 m^3/d. This phenomenon may be ascribed to two reasons. First, all adjacent wells in group S-128 interfered with each other after the horizontal well was infilled, resulting in faster CBM desorption efficiency. Second, the propagation dynamics in the reservoir fracture channels increased, causing the unblocking of the previously partially blocked fractures, which corresponds with the observations of Liu et al. (2018a).

4.2.2. Vertical wells

Owing to the low geological requirements and the simplicity of the exploitation technique, vertical wells have become a common infilling method for low-CBM producing areas (Wang and Qin, 2019; Dejam et al., 2018). The well group S-114, with a coal seam thickness ranging 5.70–6.15 m, well depth between 725 and 775 m, and gas content between 9.83 and 20.32 m^3/t, was located at the anticline core with relatively low permeability. This

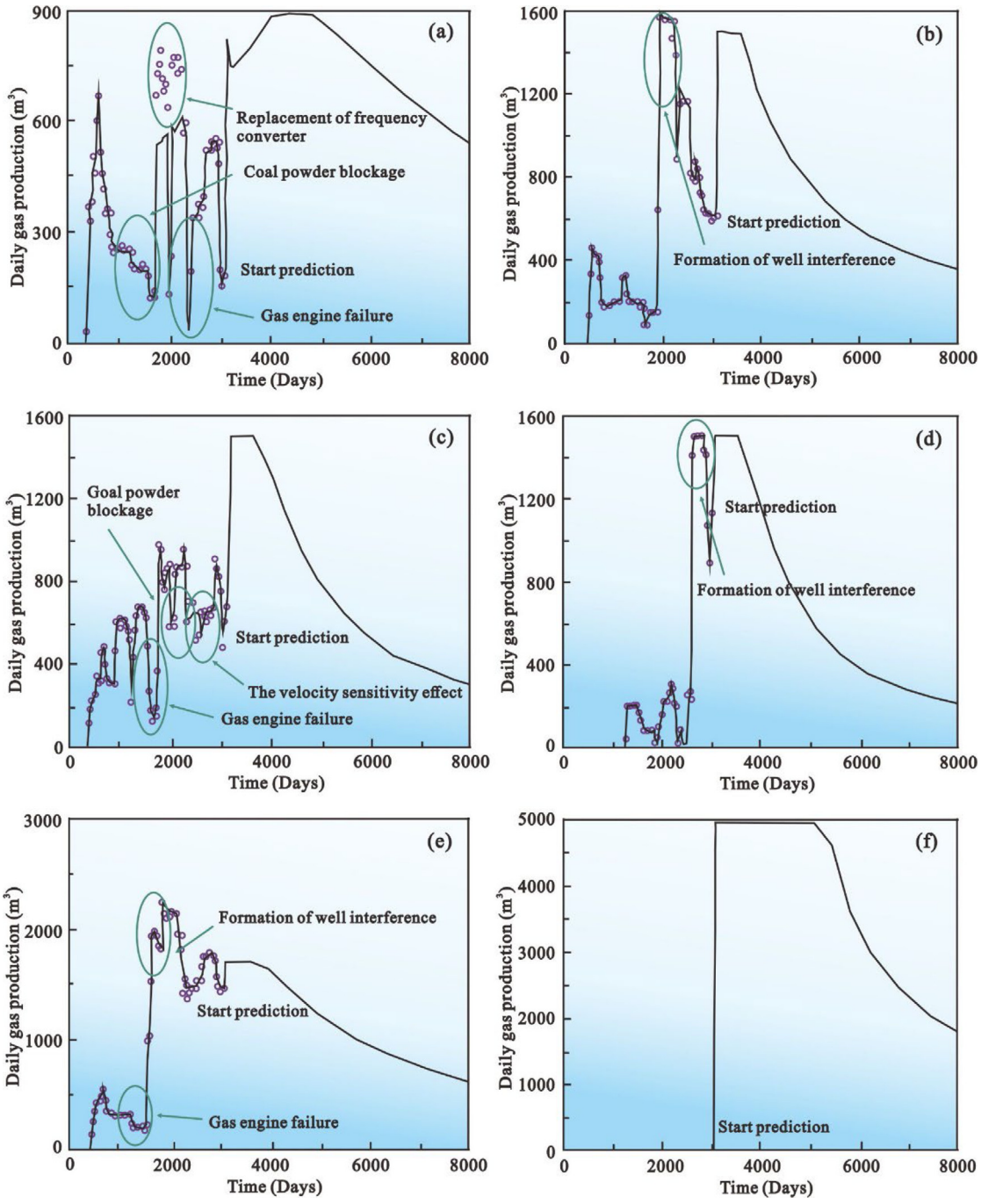

Fig. 9. The actual daily gas production and simulation fitting results of well group S-128 during the drainage process. (a), (b), (c), (d), (e), and (f) indicate wells S-128, S-024, S-025, S-129, S-031, and S-128-H1, respectively, where S-128-H1 is a newly infilled horizontal well. The circles represent the actual daily gas production of the CBM wells, while the solid lines represent the simulation-fitting results.

well group started with consistently low gas production until the secondary fracturing wells (S-114, S-115, and S-016) increased gas production. Therefore, to stimulate the overall productivity, a vertical well can be infilled in the middle of well group S-114 (see Fig. 8b). This would not only facilitate the formation of interference throughout the well group but also improve the regional CBM recovery rate. For the drainage condition, all wells produced gas at less than 520 m^3/d after casing hold pressure (as shown in Fig. 10), with wells S-114, S-115, and S-016 producing gas at a maximum rate of 963, 939, and 1157 m^3/d, respectively, following secondary fracturing of the reservoir (Fig. 10a, b, and d) and well S-131 producing gas at a maximum rate of 875 m^3/d (Fig. 10e). However, the high gas production in all wells was only sustained for a short period.

As shown in Fig. 10, after infilling the vertical well in well group S-114, the gas production of wells S-114, S-010, S-016, and S-131 increased by 425, 268, 271, and 372 m^3/d, respectively (Fig. 10a, c, d, and e), and well S-115 could maintain production of ~930 m^3/d for a long time (Fig. 10b). The newly infilled well S-114-V1 also produced gas at an average of 1008 m^3/d (Fig. 10f). These results can be attributed to the fact that the newly added well interfered with the old wells, promoting pressure drop propagation in the long- and short-axis directions (Mora and Wattenbarger, 2009), which in turn led to the original

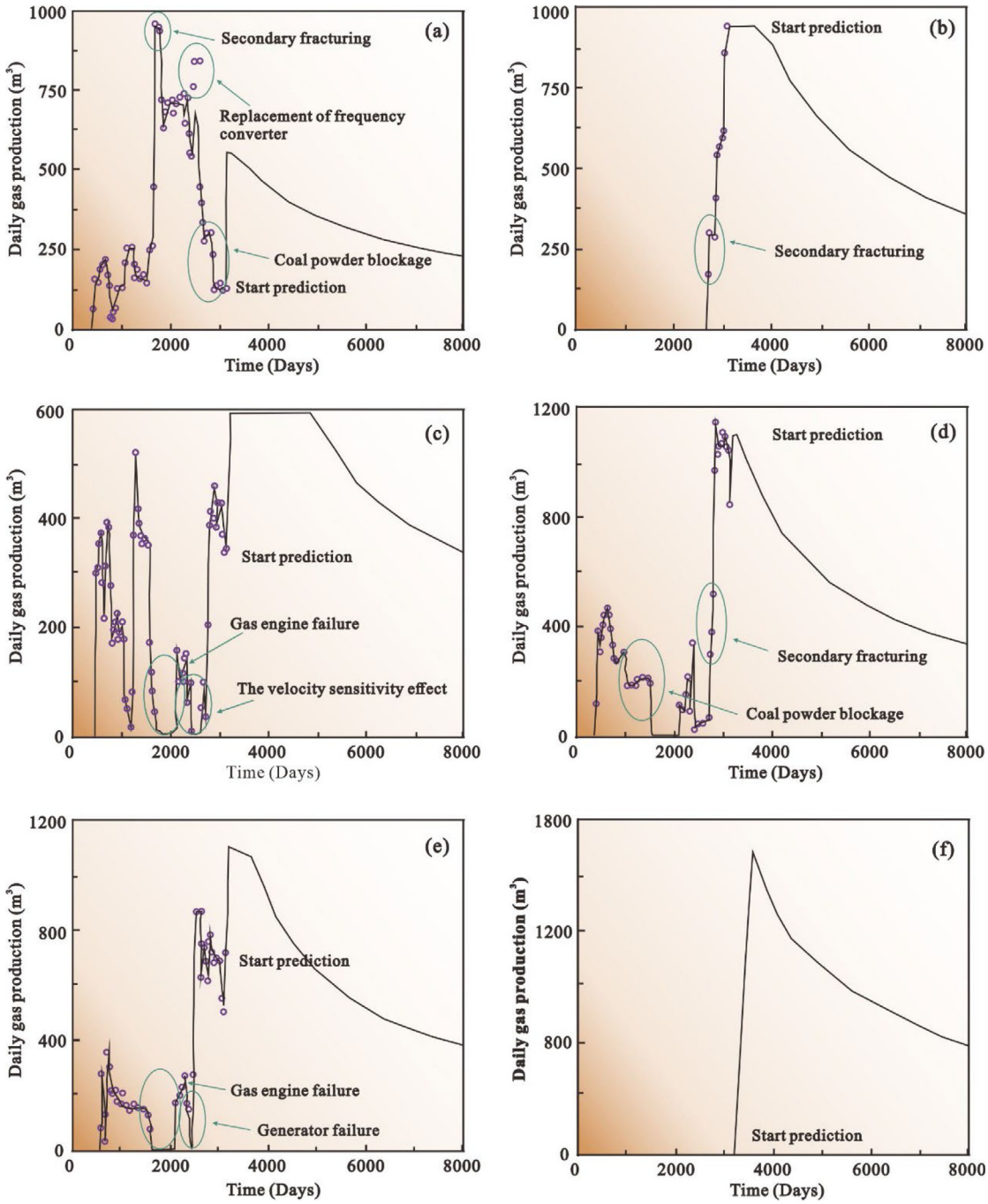

Fig. 10. The actual daily gas production and simulation fitting results of well group S-114 during the drainage process. (a), (b), (c), (d), (e), and (f) indicate wells S-114, S-115, S-010, S-016, S-131, and S-114-V1, respectively, where S-114-V1 is a newly infilled vertical well. The circles represent the actual daily gas production of the CBM wells, while the solid lines represent the simulation-fitting results.

adjacent wells interfering with each other and increasing the CBM drainage area.

4.2.3. Permeability variations

The changes in permeability before and after well pattern infilling are shown in Fig. 11. For the HP-WW (Fig. 11a), the infill well resulted in 11%–39% permeability increment compared with initial permeability (the average permeability changed from 1.58 to 2.18 mD); however, the permeability of the entire well group increased by an average of 0.24 mD after infilling a vertical well in the LP-WW (Fig. 11b). This indicates that inter-well interference can increase reservoir permeability and confirms that interference can suppress the three effects of velocity sensitivity, water sensitivity, and water lock. As shown in Fig. 11, a reservoir with high permeability exhibits high gas production potential, and the formation of inter-well interference is more conducive to capacity release. Additionally, the infilled horizontal wells allow for a greater overlap of pressure drop funnels in adjacent wells, which better facilitates connections between hydraulic and natural fractures.

In conclusion, permeability changes dynamically during CBM drainage. After infilling horizontal or vertical wells, a series of geological effects occur in the reservoir pore fractures and fluids as the water and gas saturation continue to change, making permeability changes even more complex (Liu et al., 2018a; Cai et al.,

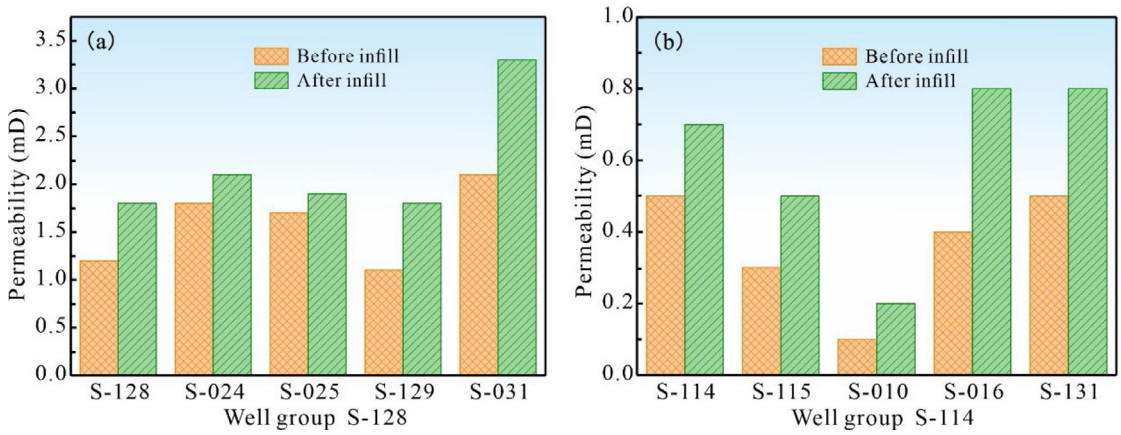

Fig. 11. The changes in permeability before and after well pattern infilling. (a) infilling a horizontal well for well group S-128; (b) infilling a vertical well for well group S-114.

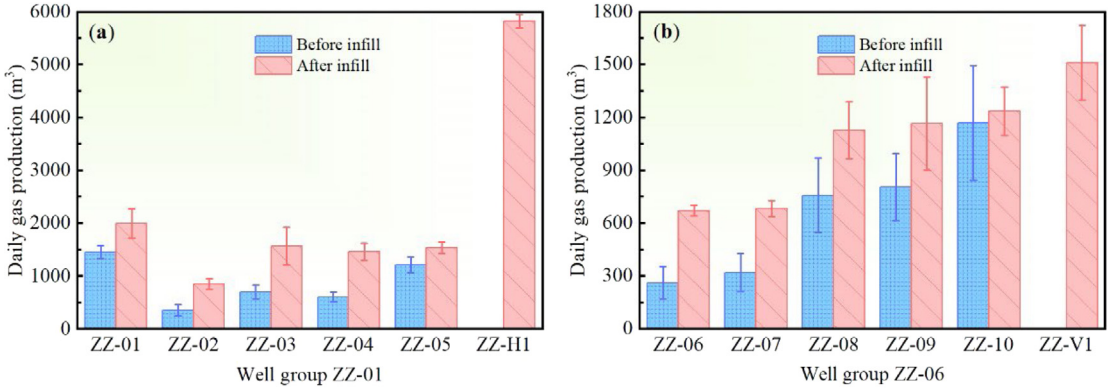

Fig. 12. Actual gas production in the Zhengzhuang Block after infilling CBM wells in the HP-WW and LP-WW reservoirs to form wells interference. The coal reservoir in well group ZZ-01 belongs to HP-WW, and the gas production after infilling a horizontal well is shown in (a); the coal reservoir in well group ZZ-06 belongs to LP-WW, and the gas production after infilling a vertical well is shown in (b).

2014). Notably, not all well pattern infilling increases permeability. When the density of the well pattern is below the critical level, this infill method facilitates the increase in reservoir permeability. Conversely, this can cause "gas stringing", significantly reducing reservoir permeability.

4.2.4. Field case

The geological settings of the Zhengzhuang and Shizhuangnan blocks, which are both located in the southern Qinshui Basin, are very similar (Wang et al., 2016). Both blocks are within a tectonic framework of wide syncline trending almost NNE, with similar coal metamorphism and depositional environments; the primary gas source is coal seam 3#, which primarily develops tensional and shear fractures and generally has medium connectivity. The differences in coal composition in the vertical and lateral directions directly cause heterogeneous microfracture development, which in turn affects the spatial variations in reservoir permeability (Cai et al., 2014; Karacan, 2013). Therefore, selecting infilled well groups similar to the HP-WW and LP-WW at Zhengzhuang provides a good reference for the Shizhuang productivity situation. As shown in Fig. 12, after infilling a horizontal well in well group ZZ-01, the gas production of wells ZZ-01, ZZ-02, ZZ-03, ZZ-04, and ZZ-05 increased by ∼546, ∼495, ∼871, ∼858, and ∼321 m^3/d, respectively, the newly infilled horizontal well produced gas at a rate of ∼5826 m^3/d (Fig. 12a). For well group ZZ-06, the gas production of wells ZZ-06, ZZ-07, ZZ-08, ZZ-09, and ZZ-10 increased by ∼409, ∼362, ∼369, ∼361, and ∼67 m^3/d, respectively, with the newly infilled vertical well ZZ-V1 producing gas at a rate of ∼1511 m^3/d (Fig. 12b). This successful case indirectly verifies the accuracy of the Shizhuang Block infilling simulation results while providing theoretical references for productivity enhancement in different reservoir types.

4.3. Analysis of interference mechanism

Inter-well interference is essentially the superposition of pressure drop propagation among adjacent wells, which generates energy migration through the pressure drop. This results in an increased pressure difference between the reservoir fluid and the wellbore, thereby enhancing the dynamics of methane desorption from the pore surface and gas migration from the fracture (Rice et al., 2008; Karacan, 2013). Fig. 12 shows the reservoir pressure drop superposition and microfluidic geological effects both before and after the well interference. The magnitude of the pressure drop propagation before interference was small, which was dominated by water transfer in the macro fracture system, consistent with the study by Wang et al. (2019). After interference, the pressure drop propagation strengthened in the longitudinal direction, and the funnel-shaped coupling accelerated. The reservoir pressure drop transitioned from water transfer to gas transfer and gradually evolved until gas transfer was dominant (see Fig. 13a). Briefly, inter-well interference can promote CBM desorption while improving the transfer efficiency of gas and liquid phase materials in the pore fracture.

During the drainage process, fluid migration within fractures is bound to carry some solid particles (e.g., coal powder and proppant) (Meng et al., 2018), which can block the throat owing

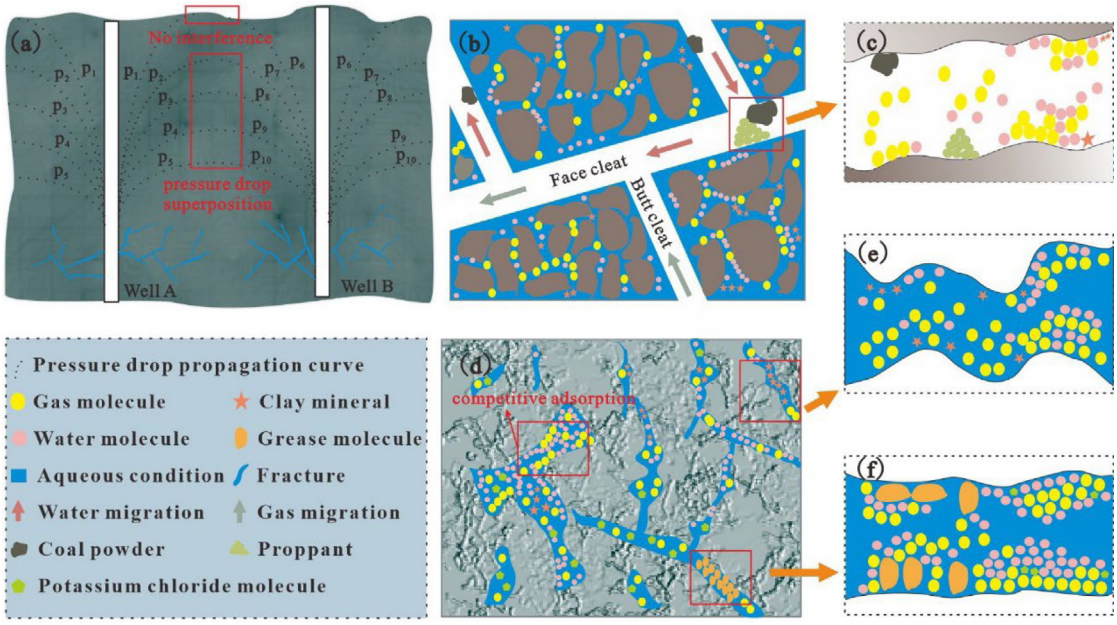

Fig. 13. Reservoir pressure drop superposition and microfluidic geological effects before and after wells interference. (a) shows the superposition of pressure drop propagation; (b) shows the velocity sensitivity effect during the drainage process, which is shown in (c) after being attenuated by inter-well interference; (d) shows the water sensitivity and water lock effects occurring during gas migration, both of which are shown in (e) and (f) after being attenuated by inter-well interference, respectively.

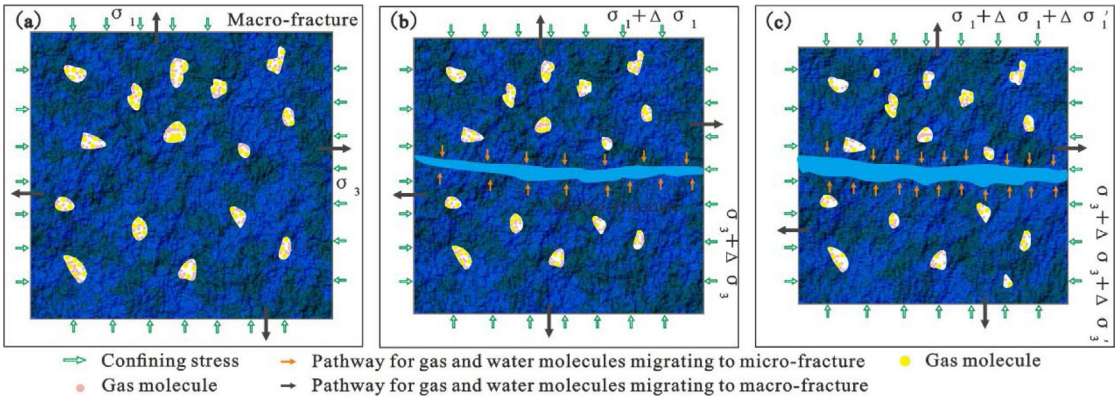

Fig. 14. Diffusion behavior of gas in the coal matrix before and after wells interference. (a) in the original state; (b) and (c) show the diffusion behavior of the gas before and after the wells interference, respectively. Although the effective stress increases after the formation of interference, the matrix shrinkage accelerates, and the pore pressure increases simultaneously, that is, the positive effect of elastic self-regulation is relatively greater than the negative effect.

to the changes in fluid flow velocity, thereby causing the particles to migrate to the large fractures (Connell et al., 2016; Yang et al., 2018b). This generates the velocity sensitivity effect (Fig. 13b), as well as the water sensitivity effect, which is caused by the expansion of clay minerals, and the water lock effect, which is due to the increased saturation of immiscible fluids in the porous medium (Fig. 13d). The water sensitivity and water lock effects lead to a decrease in reservoir permeability and desorption rate. When CBM wells interfere with each other, reservoir fracture expansion occurs, and fluid drainage dynamics increase. This facilitates the unblocking of the throat and the drainage of external immiscible fluids (Fig. 13c, e, and f), resulting in a reduction of the gas propagation resistance, which in turn suppresses the velocity sensitivity, water sensitivity, and water lock effects.

As shown in Fig. 14, well interference can promote the diffusion behavior of the gas in the matrix. Before interference formation, gas primarily flowed to macro-fractures, supplemented by micro-fractures (Fig. 14a and b); however, the reservoir indirectly controlled the gas flow via the elastic self-regulation effect created by the confining stress and matrix shrinkage (Mazumder et al., 2012; Liu et al., 2021). Although increased confining pressure led to increased effective stress and decreased pore size after interference formation, increased pore pressure facilitated increases in both the fracture scale and effective diffusion area (Fig. 14c). In comparison, the positive effect of pore pressure was greater than the negative effect caused by the confining stress. The mean free path of gas molecules decreased with increasing pore pressure (Liu et al., 2018a), implying that the primary diffusion resistance will switch from collisions between gas molecules and the pore wall (Knudsen diffusion) to collisions among gas molecules (Fick diffusion).

The advantage of this study is to construct mathematical models of pressure propagation that are more consistent with objective reality by fully considering the difference between the original permeability and post-fracturing permeability. The optimal well spacing for different types of reservoirs is quantified based on the drainage characteristics of high or low permeability reservoirs, followed by verification of the analysis through CBM

well cases in the field. Because reservoir sensitivity is affected by infilling horizontal and vertical wells in the well pattern, we reveal the suppression effect of inter-well interference on velocity sensitivity, water sensitivity, and water lock, which has not been reported in previous studies. Additionally, the mechanism of inter-well interference on the change of gas in coal from Knudsen diffusion to Fick diffusion is characterized to enrich the diffusion dynamics of CBM. Unfortunately, this study does not precisely quantify the effect of inter-well interference on the suppression of velocity sensitivity, water sensitivity, and water lock, especially for complex reservoirs with surrounding rock water supply.

The water supply in the surrounding rock affects the pressure drop propagation in the coal reservoir, resulting in diverse inter-well interference, which is not investigated in this work. Affected by external fluids, the variation of methane seepage and diffusion is more complicated in the reservoirs with surrounding rock water supply after the formation of inter-well interference. Considering the energy loss balance, the necessity of infilling horizontal and vertical wells in this type of reservoir needs further discussion. Moreover, how the sensitivity of reservoirs with surrounding rock water supply changes after the formation of inter-well interference also requires detailed analysis. Also, these studies are the goal of our next work.

5. Summary and conclusions

In this study, two types of reservoirs, the HP-WW and LP-WW, were classified based on formation permeability. The changes in productivity and permeability after infilling horizontal or vertical wells in different types of reservoirs were analyzed. Additionally, the infill adjustment methods and results were validated based on successful field cases. Considering the micro-geological effects, the inter-well interference mechanisms of the different reservoirs were analyzed in conjunction with production data and models. The following conclusions were drawn:

(1) Some CBM wells in the HP-WW formed inter-well interference, demonstrating faster pressure drop propagation efficiencies; however, none of the CBM wells in the LP-WW formed interference, indicating a lower methane desorption efficiency.

(2) As the water and gas saturation continues to change, a series of geological effects occur in reservoir pore fractures and fluids after infilling horizontal or vertical wells. For the HP-WW, the infill well resulted in 11%–39% permeability increment compared with initial permeability (the average permeability changed from 1.58 to 2.18 mD), while the permeability of the entire well group increased by an average of 0.24 mD after infilling a vertical well in the LP-WW.

(3) After the formation of inter-well interference in CBM wells, reservoir fracture expansion occurred, accompanied by an increase in fluid drainage dynamics. This facilitated the unblocking of the throat and drainage of external immiscible fluids, resulting in reduced gas propagation resistance. This, in turn, suppressed the velocity sensitivity, water sensitivity, and water lock effects. For gas diffusion dynamics, the mean free path of gas molecules decreased with increasing pore pressure, implying that the main diffusion resistance switched from collisions between gas molecules and pore wall to collisions among gas molecules, that is, Knudsen diffusion to Fick diffusion.

(4) In the study area, coal reservoirs are classified into two types with and without surrounding rock water supply. The water supply in the surrounding rock affects the pressure drop propagation in the coal reservoir, resulting in diverse inter-well interference. Due to the influence of foreign fluid, the changes in methane seepage, diffusion and sensitivity are complicated in reservoirs with surrounding rock water supply after the formation of inter-well interference. Also, these works are the goal of our future research.

Nomenclature

K	Absolute permeability of the coal rock [mD]
K_{rg}	Relative permeabilities of gas [mD]
K_{rw}	Relative permeabilities of water [mD]
S_g	Gas saturation values
S_w	Water saturation values
ρ_g	The density of gas [kg/m^3]
ρ_w	The density of water [kg/m^3]
μ_g	The viscosity of gas [mPa s]
μ_w	The Viscosity of water [mPa s]
D_f	Diffusion coefficient [m^2/s]
C_f	Volume concentration
g	Acceleration due to gravity [m/s^2]
H	Depth calculated from the base level [m]
φ	Porosity of coal-rock
t	Seepage time [s]
K_0	Initial permeability [mD]
φ_0	Initial porosity
$P_c\ (S_w)$	Capillary pressure [MPa]
$p\ \|_{r_w}$	The pressure at the bottom of the hole [MPa]
p_{Wf}	Bottom hole pressure at time t [MPa]
$p\ \|_{\Gamma}$	The pressure at the gas reservoir boundary [MPa]
f	Given function of the pressure p at time t
$q_{w,h}$	Total output
$T_{w,i}$	The conductivity of each grid
$M_{p,i}$	The fluidity ratio of the fluid in the ith grid
p_e	Formation pressure [MPa]
p_{wf}	The pressure at the grid where the root is located [MPa]
R_{x1}	The long-axis influence radius at the single-phase flow stage [m]
R_{y1}	The short-axis influence radius at the single-phase flow stage [m]
R_{x2}	The long-axis influence radius at the gas–water two-phase flow stage [m]
R_{y2}	The short-axis influence radius at the gas–water two-phase flow stage [m]
R_{x3}	The long-axis influence radius at the constant pressure production stage [m]
R_{y3}	The short-axis influence radius at the constant pressure production stage [m]
S_0	The drawdown of the hydrodynamic surface at the single-phase flow stage [m]
S_1	The drawdown in the effective support range [m]
S_{x1}	The drawdown in the long-axis fracture extension direction [m]
h	The thickness of the aquifer [m]
k_{d1}	The permeability coefficient in the support range [m/d]
k_{lc}	The permeability of the long-axis fracturing section [mD]
k_c	Post-fracturing permeability [mD]
S_{x2}	The drawdown in the low gas production stage [m]
S_{dg1}	The drawdown in the gas–water two-phase flow [m]
t_{rcg}	The time of constant pressure in the long-axis direction [d]
t_{rdg}	The time of constant pressure in the short-axis direction [d]
a_x	The fitting slope of the pressure drop along the long-axis
b_x	The fitting constant of the pressure drop along the long axis

a_y	The fitting slope of the pressure drop along the short-axis
b_y	The fitting constant of the pressure drop along the short-axis
k_{rwc}	The water-phase relative permeability in the long-axis direction [mD]
k_{rwd}	The water-phase relative permeability in the short-axis direction [mD]
x	Long-axis direction
y	Short-axis direction
z	Vertical direction

CRediT authorship contribution statement

Qifeng Jia: Writing – original draft, Investigation, Software, Validation. **Dameng Liu:** Conceptualization, Methodology, Supervision, Funding acquisition. **Xiaoming Ni:** Writing – review & editing. **Yidong Cai:** Methodology, Funding acquisition, Writing – review & editing. **Yuejian Lu:** Writing – review & editing, Software. **Zongyuan Li:** Providing data & validation, Real-time monitoring. **Yingfang Zhou:** Methodology, Software.

Declaration of competing interest

The authors declare that they have no known competing financial interests or personal relationships that could have appeared to influence the work reported in this paper.

Acknowledgments

This research was funded by the National Natural Science Foundation of China (grant nos. 41830427, 42130806 and 41922016), 2021 Graduate Innovation Fund Project of China University of Geosciences, Beijing (grant no. ZD2021YC035) and the Fundamental Research Funds for Central Universities, China (grant no. 2-9-2021-067). We are very grateful to the reviewers and editors for their valuable comments and suggestions.

References

Aminian, K., Ameri, S., 2009. Predicting production performance of CBM reservoirs. J. Natl. Gas Sci. Eng. 1, 25–30.
Andrew, B., Willem, L.B., Cristina, P., 2006. Coalbed methane resources and reservoir characteristics from the Alberta Plains, Canada. Int. J. Coal Geol.. 65, 93–113.
Cai, Y.D., Li, Q., Liu, D.M., Zhou, Y.F., Lv, D.W., 2018. Insights into matrix compressibility of coals by mercury intrusion porosimetry and N_2 adsorption. Int. J. Coal Geol. 200, 199–212.
Cai, Y.D., Liu, D.M., Mathew, J.P., Pan, Z.J., Elsworth, D., Yao, Y.B., Li, J.Q., Guo, X.Q., 2014. Permeability evolution in fractured coal-combining triaxial confinement with X-ray computed tomography, acoustic emission and ultrasonic techniques. Int. J. Coal Geol. 122, 91–104.
Cai, Y.D., Liu, D.M., Yao, Y.B., Li, J.Q., Qiu, Y.K., 2011. Geological controls on prediction of coalbed methane of (3) coal seam in Southern Qinshui Basin, North China. Int. J. Coal Geol 88, 101–112.
Clarkson, C.R., 2009. Case study: production data and pressure transient analysis of Horseshoe Canyon CBM wells. J. Can. Petrol. Technol. 48, 27–38.
Clarkson, C.R., Qanbari, F., 2016. A semi-analytical method for forecasting wells completed in low permeability, undersaturated CBM reservoirs. J. Natl. Gas Sci. Eng. 30, 19–27.
Connell, L.D., Mazumder, S., Sander, R., Camilleri, M., Pan, Z.J., Heryanto, D., 2016. Laboratory characterization of coal matrix shrinkage, cleat compressibility and the geomechanical properties determining reservoir permeability. Fuel 168, 499–512.
Cramer, B., Poelchau, H.S., Gerling, P., Lopatin, N.V., Littke, R., 1999. Methane released from groundwater: the source of natural gas accumulations in Northern West Siberia. Mar. Pet. Geol. 16, 225–244.
Davudov, D., Moghanloo, R.G., 2018. Impact of pore compressibility and connectivity loss on shale permeability. Int. J. Coal Geol. 187, 98–113.
Dejam, M., Hassanzadeh, H., Chen, Z., 2018. Semi-analytical solution for pressure transient analysis of a hydraulically fractured vertical well in a bounded dual-porosity reservoir. J. Hydrol. 565, 289–301.
Guo, C., Qin, Y., Han, D., 2017. Interlayer interference analysis based on trace elements in water produced from coalbed methane wells: a case study of the Upper Permian coal-bearing strata, Bide-Santang Basin, western Guizhou, China. Arab. J. Geosci. 10, 137–148.
Harrison, S.M., Gentzis, T., Payne, M., 2006. Hydraulic, water quality, and isotopic characterization of late cretaceous–tertiary ardley coal waters in a key test-well, Pembina–Warburg exploration area, Alberta, Canada. Br. Can. Petrol. Geol. 54, 238–260.
Hoffman, B.T., Caers, J., 2005. Regional probability perturbations for history matching. J. Pet. Sci. Eng. 46, 53–71.
Ibrahim, A.F., Nasr-El-Din, H.A., 2015. A comprehensive model to history match and predict gas/water production from coal seams. Int. J. Coal Geol. 146, 79–90.
Jia, L., Peng, S.J., Xu, J., Yan, F.Z., 2021. Interlayer interference during coalbed methane coproduction in multilayer superimposed gas-bearing system by 3D monitoring of reservoir pressure: An experimental study. Fuel 304, 121472.
Ju, Y., Xi, C.D., Wang, S.J., Mao, L.T., Wang, K., Zhou, H.W., 2021. 3-D fracture evolution and water migration in fractured coal under variable stresses induced by fluidized mining: In situ triaxial loading and CT imaging analysis. Energy Rep. 7, 3060–3073.
Kang, Y.S., Jiang, S.Y., Deng, Z., Ma, Y.Z., Wang, J., Gu, J.Y., Sun, H.S., 2020. Non-monotonic decrease of coal permeability with depth in highly compressional tectonic settings: A case study in the Bide-Santang Basin, SW China. Mar. Pet. Geol. 116, 104321.
Karacan, C.Ö, 2013. Production history matching to determine reservoir properties of important coal groups in the Upper Pottsville formation, Brookwood and Oak Grove Fields, Black Warrior Basin, Alabama. J. Natl. Gas Sci. Eng. 10, 51–67.
Keller, L.M., Schuetz, P., Erni. R, M.D., Lucas, F., Gasser, P., Holzer, L., 2016. Characterization of multi-scale microstructural features in opalinus clay. Microporous Mesoporous Math. 170, 83–94.
Kumar, H., Elsworth, D., Mathews, J.P., Marone, C., 2016. Permeability evolution in sorbing media: analogies between organic-rich shale and coal. Geofluids 16, 43–55.
Liu, T., Lin, B.Q., Fu, X.H., Gao, Y.B., Kong, J., Zhao, Y., Song, H.R., 2020. Experimental study on gas diffusion dynamics in fractured coal: A better understanding of gas migration in in-situ coal seam. Energy 195, 117005.
Liu, H.H., Sang, S.X., Xue, J.H., Lan, T.H., Xu, H.J., Ren, B., Liu, S.Q., 2018a. Evolution and geochemical characteristics of gas phase fluid and its response to inter-well interference during multi-well drainage of coalbed methane. J. Pet. Sci. Eng. 162, 491–501.
Liu, J., Yao, Y.B., Liu, D.M., Xu, L.L., Elsworth, D., Huang, S.P., Luo, W.J., 2018b. Experimental simulation of the hydraulic fracture propagation in an anthracite coal reservoir in the southern Qinshui basin, China. J. Petrol. Sci. Eng. 168, 400–408.
Liu, D.M., Zou, Z., Cai, Y.D., Qiu, Y.K., Zhou, Y.F., He, S., 2021. An updated study on CH_4 isothermal adsorption and isosteric adsorption heat behaviors of variable rank coals. J. Nat. Gas Sci. Eng. 89, 103899.
Majdi, A., Hassani, F.P., Nasiri, M.Y., 2012. Prediction of the height of destressed zone above the mined panel roof in longwall coal mining. Int. J. Coal Geol. 98, 62–72.
Mazumder, S., Scott, M., Jiang, J., 2012. Permeability increase in Bowen Basin coal as a result of matrix shrinkage during primary depletion. Int. J. Coal Geol. 96-97, 109–119.
Meng, S.Z., Li, Y., Wang, L., Wang, K., Pan, Z.J., 2018. A mathematical model for gas and water production from overlapping fractured coalbed methane and tight gas reservoirs. J. Pet. Sci. Eng. 171, 959–973.
Moore, T.A., 2012. Coalbed methane: a review. Int. J. Coal Geol. 101, 36–81.
Mora, C.A., Wattenbarger, R.A., 2009. Comparison of computation methods for CBM production performance. J. Can. Pet. Technol. 48, 42–48.
Ni, X.M., Jia, Q.F., Wang, Y.B., 2019. The relationship between current ground stress and permeability of coal in superimposed zones of multistage tectonic movement. Geofluids 2019, 1–12.
Ni, X.M., Tan, X.B., Wang, B.Y., Fu, X.K., 2021. An evaluation method for types of low-production coalbed methane reservoirs and its application. Energy Rep. 7, 5305–5315.
Palmer, I., 2009. Permeability changes in coal: analytical modelling. Int. J. Coal Geol. 77, 119–126.
Pashin, J.C., 2007. Hydrodynamics of coalbed methane reservoirs in the Black Warrior Basin: Key to understanding reservoir performance and environmental issues. Appl. Geochem. 22, 2257–2272.
Reeburgh, W.S., Tyler, S.C., Carroll, J.L., 2006. Stable carbon and hydrogen isotope measurements on Black Sea water-column methane. Deep Sea Res. II 53, 1893–1900.
Rice, C.A., Flores, R.M., Stricker, G.D., Ellis, M.S., 2008. Chemical and stable isotopic evidence for water/rock interaction and biogentic origin of coalbed methane, Fort Union Formation, Powder River Basin, Wyoming and Montana U.S.A. Int. J. Coal Geol. 76, 76–85.
Salmachi, A., Karacan, C.Ö., 2017. Cross-formational flow of water into coalbed methane reservoirs: controls on relative permeability curve shape and production profile. Environ. Earth Sci. 76, 200–216.

Shi, J.T., Wang, S., Zhang, H., Sun, Z., Hou, C.H., Chang, Y.C., Xu, Z.Z., 2018. A novel method for formation evaluation of undersaturated coalbed methane reservoirs using dewatering data. Fuel 229, 44–52.
Smith, J.W., Gould, K.W., Rigby, D., 1982. The stable isotope geochemistry of Australian coals. Org. Geochem. 3, 111–131.
Smith, J.W., Pallasser, J.R., 1996. Microbial origin of Australian coalbed methane. AAPG Bull. 80, 891–897.
Wang, J.L., Jia, A.L., Wei, Y.S., Qi, Y.D., Dai, Y., 2018. Laplace-domain multiwell convolution for simulating pressure interference response of multiple fractured horizontal wells by use of modified Stehfest algorithm. J. Pet. Sci. Eng. 161, 231–247.
Wang, Z.W., Qin, Y., 2019. Physical experiments of CBM coproduction: A case study in Laochang district, Yunnan province, China. Fuel 239, 964–981.
Wang, H., Yao, Y.B., Liu, D.M., Pan, Z.J., Yang, Y.H., Cai, Y.D., 2016. Fault-sealing capability and its impact on coalbed methane distribution in the Zhengzhuang field, southern Qinshui Basin, North China. J. Natl. Gas Sci. Eng. 28, 613–625.
Wang, W.S., Zhang, H.F., Zhang, Y.F., Duan, B.J., Liu, L.T., Ni, X.M., Feng, Y., 2019. Quantitative evaluation of cross-well interference among coalbed methane wells based on modified Kusakkin formula. Coal Sci. Technol. 47, 119–125.
Wayne, A.V., 2003. Geochemical signature of formation waters associated with coalbed methane. AAPG Bull. 87, 667–676.
Xu, Z.Y., Wang, R.Z., 2017. Absorption heat pump for waste heat reuse: current states and future development. Front. Energy 11, 414–436.
Yang, S.Y., Cai, Y.D., Wei, R., Zhou, Y.F., 2018b. A new fracture permeability model of CBM reservoir with high-dip angle in the southern Junggar Basin, NW China. Energy Explor. Exploit. 37, 125–143.
Yang, Z.B., Qin, Y., Wu, C.C., Qin, Z.H., Li, G., Li, C.L., 2019. Geochemical response of produced water in the CBM well group with multiple coal seams and its geological significance-A case study of the Songhe well group in Western Guizhou. Int. J. Coal Geol. 207, 39–51.
Yang, Z.B., Zhang, Z.G., Qin, Y., Wu, C.C., Yi, T.S., Li, Y.Y., Tang, J., Chen, J., 2018a. Optimization methods of production layer combination for coalbed methane development in multi-coal seams. Petrol. Explor. Dev. 45, 312–320.
Zhang, Z., Qin, Y., Bai, J.P., Li, G.Q., Zhuang, X.G., Wang, X.M., 2018. Hydrogeochemistry characteristics of produced waters from CBM wells in southern qinshui basin and implications for CBM commingled development. J. Natl. Gas Sci. Eng. 56, 428–443.
Zhao, X., Jiang, B., Xu, Q., Liu, J.G., Zhao, Y., Duan, P.P., 2016. Well pattern design and optimal deployment for coalbed methane development. Petrol. Explor. Dev. 43, 89–96.